

IONIC COMPOSITION STRUCTURE OF CORONAL MASS EJECTIONS IN AXISYMMETRIC MAGNETOHYDRODYNAMIC MODELS

B. J. LYNCH¹, A. A. REINARD², T. MULLIGAN³, K. K. REEVES⁴, C. E. RAKOWSKI⁵, J. C. ALLRED⁶, Y. LI¹,
J. M. LAMING⁵, P. J. MACNEICE⁷, AND J. A. LINKER⁸

¹ Space Sciences Laboratory, University of California, Berkeley, CA 94720, USA; blynch@ssl.berkeley.edu, yanli@ssl.berkeley.edu

² NOAA Space Weather Prediction Center, Boulder, CO 80505, USA; alysha.reinard@noaa.gov

³ Space Sciences Department, The Aerospace Corporation, Los Angeles, CA 90009, USA; tamitha.mulligan@aero.org

⁴ Harvard-Smithsonian Center for Astrophysics, Cambridge, MA 02138, USA; kreeves@cfa.harvard.edu

⁵ Space Sciences Division, Naval Research Laboratory, Washington, DC 20375, USA; c.rakowski@nrl.navy.mil, j.laming@nrl.navy.mil

⁶ Department of Physics, Drexel University, Philadelphia, PA 19104, USA; jca32@drexel.edu

⁷ NASA Goddard Space Flight Center, Greenbelt, MD 20771, USA; peter.j.macneice@nasa.gov

⁸ Predictive Sciences, Inc., San Diego, CA 92121, USA; linker@presci.com

Received 2011 April 19; accepted 2011 July 26; published 2011 October 4

ABSTRACT

We present the ionic charge state composition structure derived from axisymmetric MHD simulations of coronal mass ejections (CMEs), initiated via the flux-cancellation and magnetic breakout mechanisms. The flux-cancellation CME simulation is run on the *Magnetohydrodynamics-on-A-Sphere* code developed at Predictive Sciences, Inc., and the magnetic breakout CME simulation is run on *ARC7* developed at NASA GSFC. Both MHD codes include field-aligned thermal conduction, radiative losses, and coronal heating terms which make the energy equations sufficient to calculate reasonable temperatures associated with the steady-state solar wind and model the eruptive flare heating during CME formation and eruption. We systematically track a grid of Lagrangian plasma parcels through the simulation data and calculate the coronal density and temperature history of the plasma in and around the CME magnetic flux ropes. The simulation data are then used to integrate the continuity equations for the ionic charge states of several heavy ion species under the assumption that they act as passive tracers in the MHD flow. We construct two-dimensional spatial distributions of commonly measured ionic charge state ratios in carbon, oxygen, silicon, and iron that are typically elevated in interplanetary coronal mass ejection (ICME) plasma. We find that the slower CME eruption has relatively enhanced ionic charge states and the faster CME eruption shows basically no enhancement in charge states—which is the opposite trend to what is seen in the in situ ICME observations. The primary cause of the difference in the ionic charge states in the two simulations is not due to the different CME initiation mechanisms per se. Rather, the difference lies in their respective implementation of the coronal heating which governs the steady-state solar wind, density and temperature profiles, the duration of the connectivity of the CME to the eruptive flare current sheet, and the contribution of the flare-heated plasma associated with the reconnection jet outflow into the ejecta. Despite the limitations inherent in the first attempt at this novel procedure, the simulation results provide strong evidence in support of the conclusion that enhanced heavy ion charge states within CMEs are a direct consequence of flare heating in the low corona. We also discuss future improvements through combining numerical CME modeling with quantitative ionic charge state calculations.

Key words: magnetic reconnection – magnetohydrodynamics (MHD) – Sun: corona – Sun: coronal mass ejections (CMEs) – Sun: flares – Sun: heliosphere

1. INTRODUCTION

The supersonic expansion of the solar wind into the heliosphere (Parker 1958) causes the density and temperature of the plasma continuously streaming along open field lines to drop rapidly as a function of distance from the Sun. A consequence of the strong radial dependence of these rapidly changing quantities and the varying chemical properties of the different heavy ion species in the solar wind is that the ionic charge states become “frozen-in” over a range of distances in the low corona (see von Steiger et al. 1997; Bochsler 2000, and references therein).

Ionic charge state measurements were first, and continue to be, used as a tool to investigate coronal heating processes that accelerate the steady-state slow and fast solar wind (e.g., Hundhausen et al. 1968; Owocki et al. 1983; Bürgi & Geiss 1986; Ko et al. 1997; Laming & Lepri 2007). Additionally, their application to periods of transient solar wind flow typically associated with interplanetary coronal mass ejections (ICMEs) has proven to be quite useful, both as identifying signatures of ICMEs, and in estimating the coronal temperature conditions of the ICME source region (e.g., Bame et al. 1979; Fenimore 1980;

Henke et al. 1998; Lepri et al. 2001; Lepri & Zurbuchen 2004, 2010; Rakowski et al. 2007, 2011; Gruesbeck et al. 2011).

ICMEs are often associated with unusual ionic charge state composition, indicating a thermal environment during the coronal mass ejection (CME) initiation that is very different from that of the ambient solar wind (Galvin 1997; von Steiger et al. 2000; Richardson & Cane 2004; Zurbuchen & Richardson 2006, and references therein). CMEs are routinely associated with erupting prominences or disappearing filaments. Emission line observations of prominence/filament material indicate much cooler temperatures ($\sim 10^4$ K) than the surrounding corona (~ 1 MK), which may lead one to predict anomalously low charge states in ICMEs that are associated with erupting prominences/filaments. Observations of He^+ , not usually found in the solar wind, are indicative of such periods, but have only been seen in a handful of events (Schwenn et al. 1980; Zwickl et al. 1983; Burlaga et al. 1998; Skoug et al. 1999; Gloeckler et al. 1999). However, recent analyses by Lepri & Zurbuchen (2010) have examined measures of low charge states in carbon, oxygen, and iron and showed—largely thanks to the increased temporal

resolution—that approximately 4% of ICMEs contain in situ signatures consistent with filament-like temperatures. This represents a much larger fraction than previous estimates and, in ICMEs with coherent magnetic structure (magnetic clouds), the occurrence rates of low charge states are much higher ($\sim 12\%$).

A large fraction of ICME periods are associated with measurements of unusually high charge states. High oxygen charge states were measured in ICMEs by Henke et al. (1998, 2001) and Reinard et al. (2001), showing many ICME periods are characterized by $O^{7+}/O^{6+} > 1.0$. Reinard (2005) showed a correlation between ionic charge states and the associated flare magnitude and suggested the enhanced charge states resulted from flare-related heating in the corona. Elevated iron charge states were first observed in the solar wind by Bame et al. (1979) and Fenimore (1980) during “temperature depressed” periods, now known to be ICMEs. A limitation of this earlier work was that they could only resolve iron charge states up to 16+. Moreover, with the improved measurements from the SWICS instrument (Gloeckler et al. 1992) aboard the ACE spacecraft, Lepri et al. (2001) and Lepri & Zurbuchen (2004) were able to conduct detailed studies that resolved the full range of iron charge states in CMEs. They first reported the high iron charge state ratio of $Fe^{\geq 16+}/Fe_{\text{total}} > 0.10$ as an excellent identifier of ICMEs in the solar wind and went on to show that the average iron charge state Q_{Fe} was a more robust measure in terms of instrumentation count rates. Gruesbeck et al. (2011) found that 95% of their 200 ICME sample exhibits some measurable portion of a bi-modal distribution in iron (typically with peaks at Fe^{10+} and Fe^{16+}) which is much higher than the previous estimates of $\sim 50\%$ of ICMEs having high charge states (e.g., Lepri & Zurbuchen 2004). Richardson & Cane (2004, 2010) have used the elemental and ionic composition data to develop a series of empirical functions for various “expected composition” values depending on solar wind speed, which can be used in the identification of ICME periods, analogous to their low proton temperature formulation (Richardson & Cane 1995).

Recent work by Rakowski et al. (2007) and Gruesbeck et al. (2011) has made important progress toward using the observed in situ charge state observations in ICMEs to constrain the temperature and density history of the CME plasma in the low corona. Through detailed modeling of the ionic charge state evolution in CME/ICME plasma outflow these authors have been able to conclude that, in general, the plasma needs an elevated initial density (compared to nominal coronal values for the solar wind) and must experience rapid heating (presumably flare-related) in order to offset the intrinsic rapid expansion (i.e., cooling) associated with CME eruption and propagation. Additionally, Rakowski et al. (2011) have examined the plasma heating associated with dissipation of magnetic energy during the relaxation of the CME/ICME magnetic structure, but conclude that additional heating is still required to account for the highest iron charge states ($Fe^{\geq 16+}$).

Lynch (2006) suggested that a consistent treatment of the rapid expansion associated with CME initiation and lift-off, coupled with correct energy accounting and thermodynamics in numerical CME simulations, would allow researchers to investigate whether different CME initiation models predicted differences in the distribution of heavy ion charge states or coherent spatial variations of charge state enhancements throughout the ejecta material. A similar line of reasoning has been used by a number of researchers in the investigation of spectroscopic emission in and around CMEs in the low corona in order to quantify the heating and plasma’s thermal structure during the eruption

process. Using the densities and temperatures derived by line ratios, peak emission temperatures, and coronagraph measurements from a variety of multi-wavelength observations, including the Ultraviolet Coronagraph Spectrometer (UVCS), EUV Imaging Telescope, and Large Angle and Spectrometric Coronagraph instruments aboard the *Solar and Heliospheric Observatory (SOHO)*, the SECCHI suite on *STEREO*, the EUV Imaging Spectrometer (EIS) and X-Ray Telescope (XRT) aboard *Hinode*, and others, combined with comprehensive emission modeling, work by Akmal et al. (2001), Bemporad et al. (2007), Lee et al. (2009), and Landi et al. (2010) indicate that, at least early on in the ejecta’s evolution, the energy required for heating the plasma to temperatures consistent with the observed emission signatures must be of the order of the kinetic energy of the eruption itself. Rakowski et al. (2007) drew a similar conclusion from their ionic charge state calculations. In our analysis that follows, we will concentrate on the spatial structure of heavy ion charge states in flux rope CMEs, but certainly acknowledge the potential for this type of procedure—combining magnetohydrodynamic (MHD) simulation results with the calculation of associated ionic charge state distributions—to bridge the gap between observed UV emission in the low corona and the in situ ionic composition measurements.

In this paper, we analyze the numerical MHD simulation results for two well-established CME initiation models in 2.5 dimensions: flux-cancellation and magnetic breakout. Both the flux-cancellation and magnetic breakout simulations are run with MHD codes that employ versions of the energy equation that are sufficiently realistic to account for field-aligned thermal conduction, radiative losses, and parameterized coronal heating. This not only allows the generation of an ambient solar wind but also enables us to track the energy evolution and ultimately provides a more accurate plasma temperature. This is a crucial development due to the association of elevated charge states with flare heating as a consequence of magnetic reconnection and the associated rapid conversion of free magnetic energy during the eruption. The structure of the paper is as follows: in Section 2 we briefly describe each of the MHD codes and their background solar wind and CME initiation models. In Section 3, we describe the ionic composition charge state post-processing procedure and in Section 4 we compare the spatial distribution of several heavy ion charge state ratios resulting from the flux-cancellation and magnetic breakout CME initiation and evolution in low corona. We summarize our results in Section 5 and discuss future improvements in combining quantitative charge state modeling with solar and heliospheric MHD simulations.

2. MHD MODELING OF THE SOLAR WIND AND CME ERUPTIONS

First, we will briefly report on the similarities and differences between the *Magnetohydrodynamics-on-A-Sphere (MAS)* code used to run the flux-cancellation CME simulation and *ARC7* used to run the magnetic breakout CME simulation. Second, we will briefly describe each of the initial steady-state background wind solutions and the CME eruptions through their respective model coronae. For further technical details and information on the numerical methods used in each simulation to advance the MHD equations see the following references; *MAS* is described by Mikić et al. (1999), Linker et al. (2001), and Lionello et al. (2001, 2009) and *ARC7* is described in MacNeice et al. (2004) and Allred & MacNeice (2011).

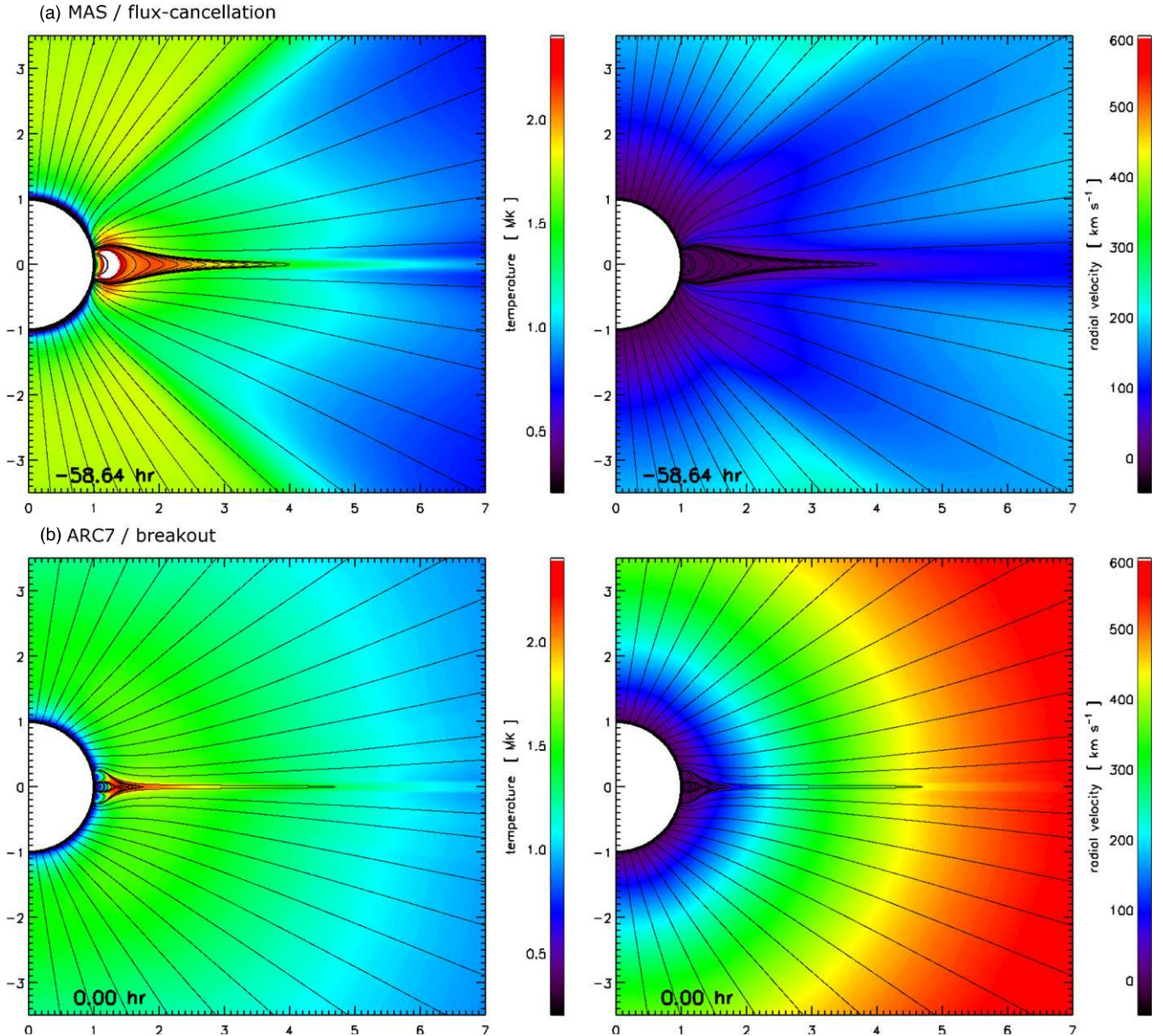


Figure 1. The top row (a) plots the *MAS* flux-cancellation background steady-state solar wind temperature (left panel) and radial velocity (right panel). The axis units are in solar radii and representative magnetic field lines are overplotted. The shifted simulation times are indicated in the lower left corner (see the text for details). The bottom row (b) plots the *ARC7* magnetic breakout quantities in the same format.

here we take $H_0 = 1.07 \times 10^{-6}$ erg cm $^{-3}$ s $^{-1}$ and $\lambda = 0.7 R_\odot$. The third term is included to model the effects of the additional heating in strong-field active regions (e.g., Lionello et al. 2009) and in the simulation presented herein we have taken $B_0 = 2.2$ G, $c_1 = 1.34 \times 10^{-5}$ erg cm $^{-3}$ s $^{-1}$, $c_2 = 1.3$, $c_3 = 0.25$, and $c_4 = 1$. The coronal heating in the *ARC7* code is parameterized as

$$\text{ARC7 : } H = \frac{H_0}{\lambda} \left(\frac{R_\odot}{r} \right)^2 e^{-(r-R_\odot)/\lambda}, \quad (13)$$

where $H_0 = 4 \times 10^5$ erg cm $^{-2}$ s $^{-1}$ and $\lambda = 0.9 R_\odot$. Since *ARC7* solves the ideal MHD equations there is no corresponding ohmic dissipation term (because $\eta = 0$). Therefore, the conversion of free magnetic energy released during the eruption into bulk plasma heating will be underestimated in the *ARC7* simulation results. We will discuss the implications for our charge state analysis in Section 5.

Figure 1 plots both the *MAS* (top row) and *ARC7* (bottom row) simulation coronae at the end of their respective relaxation phases through which each system has reached its equilibrium, steady-state solar wind solution. The left panels show the plasma temperature T and the right panels show the radial velocity. The details of the initial magnetic field configurations in the *MAS* flux-cancellation and *ARC7* breakout simulations are described in Reeves et al. (2010) and Allred & MacNeice (2011), respectively. Representative magnetic field lines are overplotted in every panel, showing that the steady-state solar wind solution results in large open-field regions at the poles, a narrow band of closed field at the equator that makes up the helmet streamer belt, and an extended radial current sheet separating the hemispheres of opposite magnetic polarity in each of the simulations. The two simulations are run with very different pre-eruption timescales. Specifically, the *MAS* simulation is run for much longer leading up to the eruption than is the *ARC7* simulation. Only during the eruption phase do the two simulations then proceed on similar

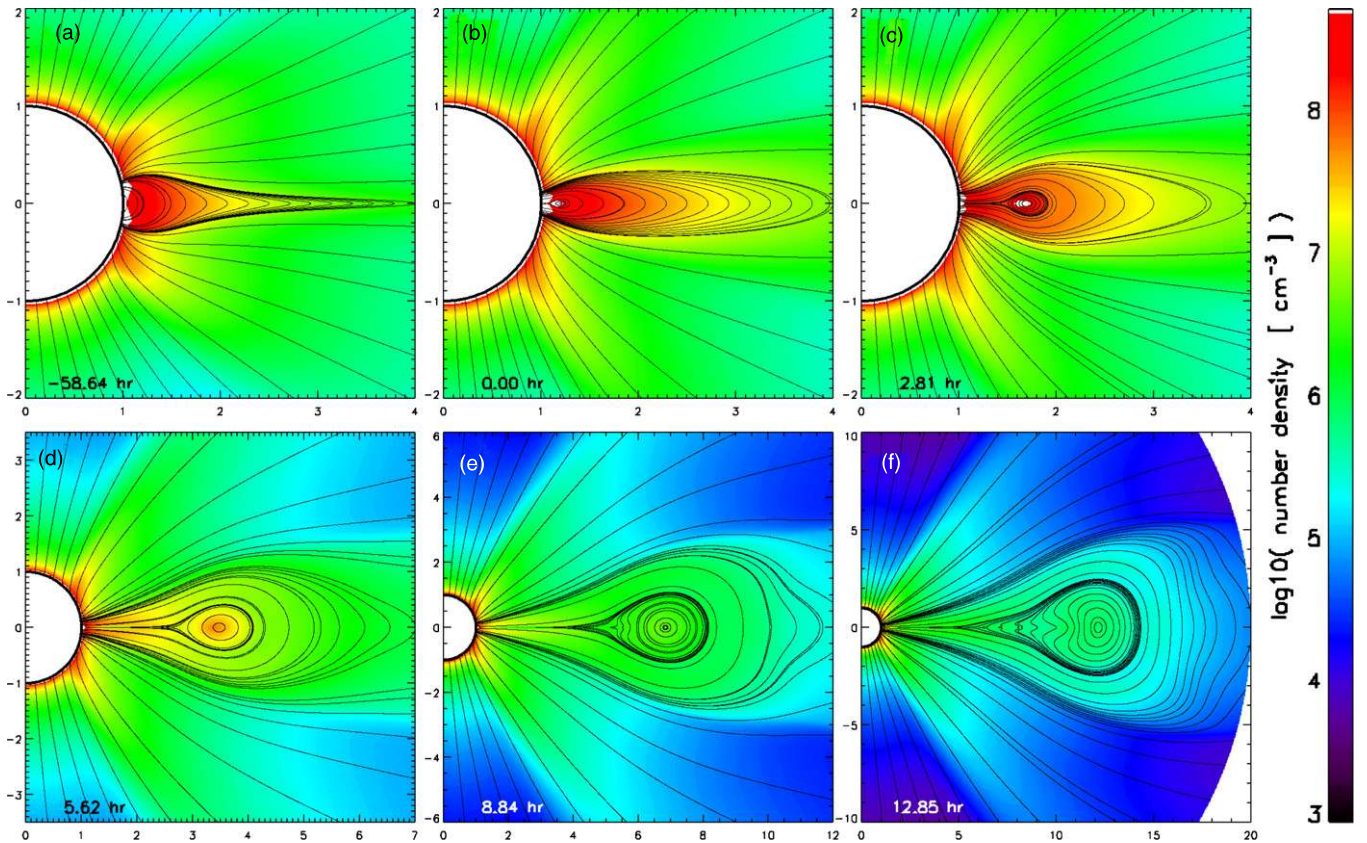


Figure 2. Magnetic field lines plotted over the logarithm of plasma number density that show the temporal evolution of the *MAS* flux-cancellation eruption.

timescales. Therefore, in order to ease the comparison of the two CME eruptions throughout the rest of the paper, we have time-shifted the *MAS* simulation by defining $t = t_R - 347\tau_A$, where $\tau_A = 1445.9$ s is the characteristic Alfvén time and t_R is the Reeves et al. (2010) simulation time. Thus, the end of the solar wind relaxation phase of the *MAS* simulation shown in Figure 1 corresponds to $t = -146\tau_A = -58.64$ hr.

The temperature and radial velocity structure of the steady-state solar wind in each simulation are significantly different. The *MAS* helmet streamer is much thicker than its *ARC7* counterpart. The effect of the *MAS* strong-field heating term is visible in the temperature's latitudinal profile; the polar region corona is approximately 1.8 MK at $2 R_\odot$, decreases toward the equator, and increases again in the vicinity of the streamer belt. The temperature in the closed-field streamer belt reaches ~ 3 MK. The *MAS* radial velocity also reflects the temperature structure; however we note that the solar wind speed is fairly slow, reaching ~ 350 km s⁻¹ by $10 R_\odot$ over the polar regions. The *ARC7* temperature and radial velocity structure are much more spherically symmetric, as expected from the symmetry in both the coronal heating (Equation (13)) and solar wind acceleration (Equation (6)). The *ARC7* corona has comparable values for the steady-state temperatures but the solar wind velocities are greater, reaching $\gtrsim 600$ km s⁻¹ by $10 R_\odot$.

There are obvious limitations to the single-fluid MHD approach to solar wind modeling inherent in our *MAS* and *ARC7* simulations. Specifically, the inclusion of helium and the coupling between the alphas, protons, and electrons has been shown to have a significant effect on various properties of the steady-state wind solutions such as the maximum coronal electron temperature and the mass fluxes at 1 AU (e.g., Bürgi 1992; Hansteen et al. 1997, and references therein). The advantage of

the large-scale MHD approach is the self-consistent evolution of the magnetic field structure of the corona and inner heliosphere, which is absolutely necessary for modeling the initiation of CMEs.

It is worth emphasizing that, despite having similar forms of the MHD equations and parameterizations for thermal conduction, radiative losses, and coronal heating, the *MAS* and *ARC7* simulations were both developed and run for purposes entirely independent of the analysis we are performing here and no attempt was made to create identical background solar wind solutions or match physical properties between the two simulations. We have applied the same post-processing procedure to calculate the ionic charge states associated with the CME eruptions in each of the simulations to demonstrate the general robustness of the technique, and will compare the results in order to discuss how certain features of each of the simulations are reflected in the resulting charge state structure. The purpose of this paper is not to determine which MHD code is superior or which CME initiation mechanism is more realistic; rather, we are presenting an analysis that can be used to fine tune some of the parameters of the MHD simulations and increase the value of existing models and modeling infrastructure by providing another set of predicted observables that can be derived from MHD simulations of the Sun and the heliosphere.

2.2. *MAS* Flux-cancellation Eruption

Figure 2 plots the evolution of the number density during the *MAS* flux-cancellation eruption along with representative magnetic field lines. The color scale is logarithmic and shown to the right of each panel, while the shifted simulation time in hours is in the lower left of each panel. The *MAS*

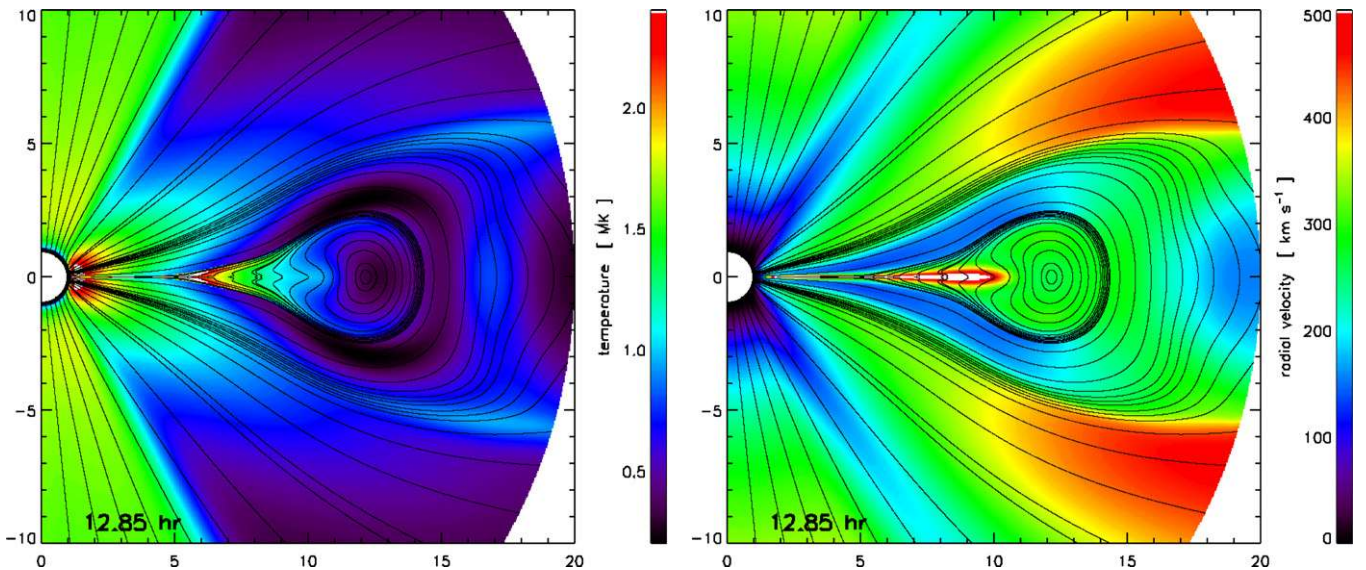


Figure 3. *MAS* flux-cancellation eruption at $t = 12.85$ hr showing the MHD proton temperature (left) and radial velocity (right) of the flux rope ejecta.

flux-cancellation eruption is described in detail by Reeves et al. (2010, and references therein), but we will briefly review some of the important features of the eruption here.

The simulation has five main phases that describe the evolution of the system up through and including the eruption. The equilibration phase is run for $200\tau_A$, allowing the system to relax to the steady-state solar wind solution shown in Figures 1 and 2(a). The shearing phase (200 – $285\tau_A$) is used to increase the magnetic energy of the system by generating a B_ϕ component above the equatorial polarity inversion line in the closed streamer belt fields. The flux-cancellation phase (285 – $305\tau_A$) is used to decrease the radial magnetic field at the inner boundary from a maximum of 10 G to 8.5 G representing a 15% decrease in radial flux which leads to the formation of a coronal flux rope in the corona anchored by a radial current sheet (e.g., see Linker et al. 2003). After the flux cancellation, the coronal flux rope is in a meta-stable state and relatively close to the loss-of-equilibrium point. During this meta-stable phase (305 – $347\tau_A$) the flux rope slowly rises as resistive diffusion slowly decreases the current density and allows magnetic reconnection to begin in the radial current sheet beneath the flux rope, destabilizing the system and marking the beginning of the eruption phase, shown in Figure 2(b). Panels 2(c)–(f) show the development of the CME eruption ($>347\tau_A$), including the radial propagation of the flux rope, and the rapid elongation of the thin, radial eruptive flare current, and the continuous transfer of magnetic flux through the flare reconnection region that simultaneously forms both the post-eruption arcades beneath the flare current sheet builds up the flux content of the erupting CME.

Figure 3 plots the plasma temperature and radial velocity during the simulation at the time of Figure 2(f). The *MAS* outer boundary is at $r = 20 R_\odot$ so the simulation data do not fill the plot area in Figures 2(f) or 3 completely. The most important features to our ionic charge state analysis that follows are the high plasma temperatures coming out of the eruptive flare reconnection jet and the process by which flare-heated plasma becomes part of the erupting structure. Besides the $>500 \text{ km s}^{-1}$ speeds in the narrow jet (the simulation data colored white correspond to values exceeding the color scale maximum), the CME flux rope itself is relatively slow with an average interior radial velocity of $\sim 300 \text{ km s}^{-1}$. The characteristic Alfvén speed

in the *MAS* simulation is 480 km s^{-1} (Reeves et al. 2010) although it varies considerably throughout the computational domain (e.g., it is on the order of 800 km s^{-1} in the stronger, closed-field region of the streamer belt before the eruption). In the analytical version of the loss-of-equilibrium model, the CME speed is determined by the magnetic energy contained in the flux rope and the magnetic reconnection rate available at the eruptive flare current sheet (e.g., Lin 2002; Reeves & Forbes 2005). While one might be tempted to characterize our flux-cancellation results as a “slow” CME launched into a slow solar wind, it is not really the most accurate or useful description because various model parameters could be modified to yield higher eruption speeds fairly easily.

2.3. ARC7 Magnetic Breakout Eruption

Figure 4 plots the evolution of the number density during the *ARC7* magnetic breakout eruption along with representative magnetic field lines in the same format as Figure 2. The various phases of the magnetic breakout CME initiation mechanism are discussed by Lynch et al. (2008, and references therein). As in the previous section, we will briefly review the important features of the eruption.

The equilibration phase is run for 10^5 s (27.78 hr) to establish the steady-state solar wind solution shown in Figure 4(a). The shearing phase starts at $t = 0$ hr in the *ARC7* simulation and lasts for 2×10^4 s (5.56 hr) with a sinusoidal temporal dependence and a maximum shearing velocity of $\sim 30 \text{ km s}^{-1}$. The central arcade of the compact multi-polar flux system that makes up the helmet streamer expands, compressing and distorting the magnetic null point and building up a current sheet along the separatrix surface separating the different flux systems. Once this current sheet has been compressed to the scale of the numerical grid the numerical errors act as diffusion (associated with an effective numerical resistivity) and allow the onset of the magnetic breakout reconnection at the overlying current sheet. The magnetic reconnection above the sheared fields allows faster expansion, driving continued reconnection, and setting up a positive-feedback situation that leads to runaway expansion and the CME eruption. Relatively early on in the eruption the original X-point separates into a large-scale

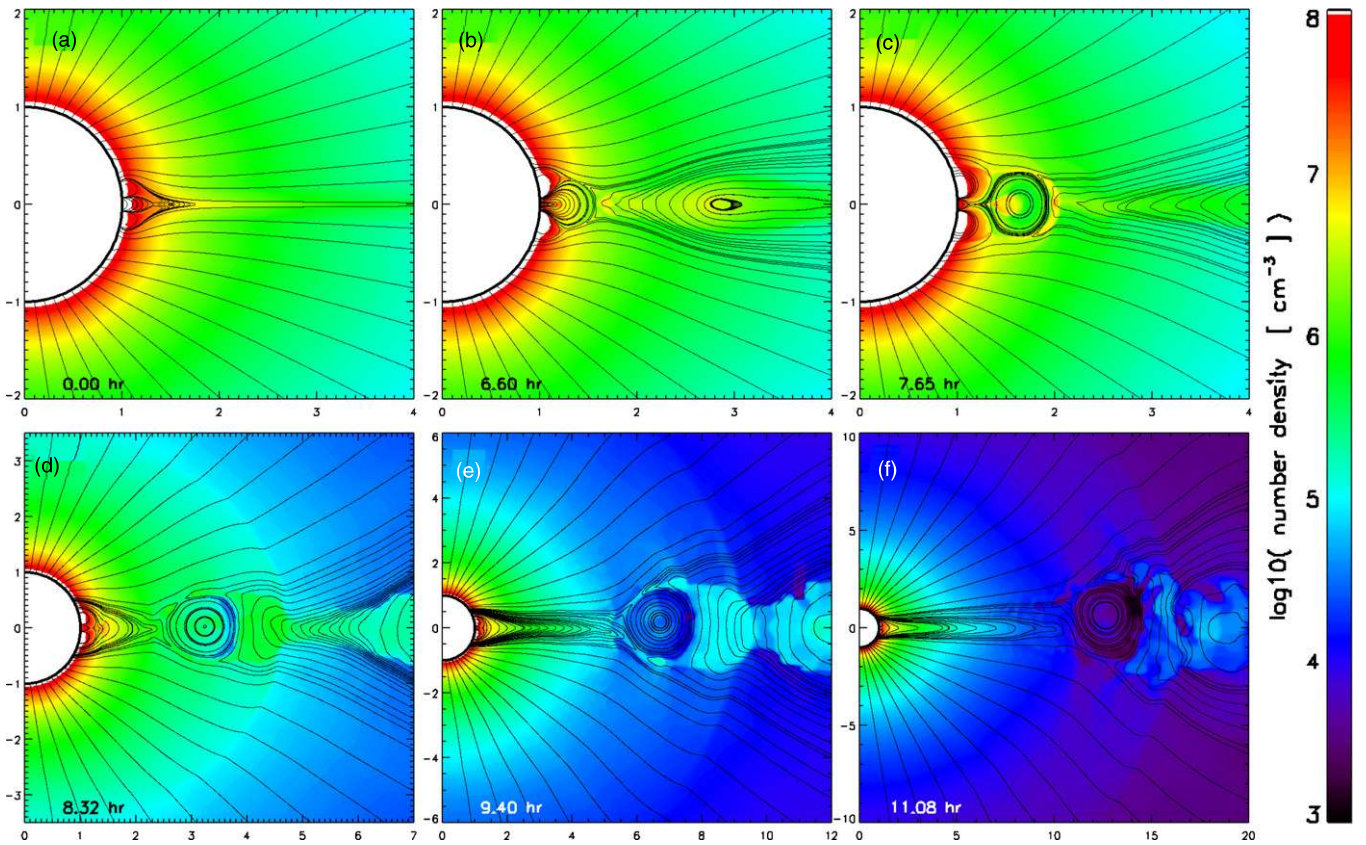


Figure 4. Temporal evolution of the *ARC7* magnetic breakout eruption, shown in the same format as Figure 2.

X-O-X-point configuration, which was also seen in previous simulations without a background solar wind (MacNeice et al. 2004). However, in the presence of a background solar wind and associated open field structure, the upper part of the heliospheric streamer becomes fully detached from the surface. This effect, seen from Figure 4(b) onward, is an artifact of the 2.5D axisymmetry and was described in detail by van der Holst et al. (2007). In fact, an analogous effect is seen in three-dimensional simulations with equatorial symmetry (van der Holst et al. 2009). The rapid expansion of the sheared field creates an extended radial current sheet beneath the sheared core setting up the standard eruptive flare current sheet configuration and facilitates the flare reconnection phase of the breakout eruption. Figure 4(c) shows the creation of highly twisted flux rope field lines out of the side-lobe fluxes being processed by the eruptive flare reconnection. Panels 4(d)–(f) show the streamer flux system rebuilding itself behind the erupting CME and the CME propagation through the low corona. Unlike the *MAS* eruption, the multi-flux topology disconnects the CME ejecta from access to the eruptive flare current sheet and its associated reconnection jets of flare-heated plasma relatively quickly.

Figure 5 plots the plasma temperature and radial velocity corresponding to Figure 4(f). The important features to note here are that the breakout CME ejecta contains, by $\sim 10 R_\odot$, very low plasma temperatures. The field lines show the topological disconnect between the higher temperature trailing streamer structure and the ejecta. Likewise, the pre-eruption streamer belt flux has become a series of giant U-loops being carried out by the breakout eruption. The radial velocities of the breakout eruption are much higher than their *MAS* counterpart. The CME interior is largely $\gtrsim 700 \text{ km s}^{-1}$, while the leading edge of the pre-eruption streamer density pile-up has speeds of $> 1000 \text{ km s}^{-1}$.

Characterizing our *ARC7* magnetic breakout results as a “fast” CME launched into a fast wind has the same basic problems associated with the analogous *MAS* classification. Antiochos et al. (1999) argued that the breakout eruption necessarily proceeds at the Alfvén speed of the system and this has been borne out in subsequent numerical simulations (MacNeice et al. 2004; DeVore & Antiochos 2008; Lynch et al. 2008). Given the large range of Alfvén speeds in the corona (which is a feature of almost every MHD model, e.g., Evans et al. 2008), we note that the *ARC7* CME speeds are higher than the *MAS* CME speeds in roughly the same proportion as the Alfvén speeds in the respective pre-eruption strong-field regions: the *ARC7* values are on the order of $1500\text{--}2000 \text{ km s}^{-1}$.

3. CALCULATING CHARGE STATES FROM THE MHD SIMULATION DATA

3.1. Tracing Individual Lagrangian Plasma Parcels

The MHD simulation results give us the global evolution of each CME eruption and their propagation through the respective background solar wind models. For any given physical position at a given simulation output time, we can integrate the bulk velocity backward in time through the simulation data cube to obtain a plasma density and temperature history for the associated Lagrangian plasma parcel. We use standard fourth-order Runge–Kutta integration (Press et al. 1992) through the (r, θ, t) coordinates. The integration routine evaluates the velocity field using linear interpolation between neighboring grid points in space and between those points in the two adjacent simulation output planes in time.

Figure 6 shows an example of the velocity integration procedure applied to both the *MAS* (top row) and *ARC7* (bottom

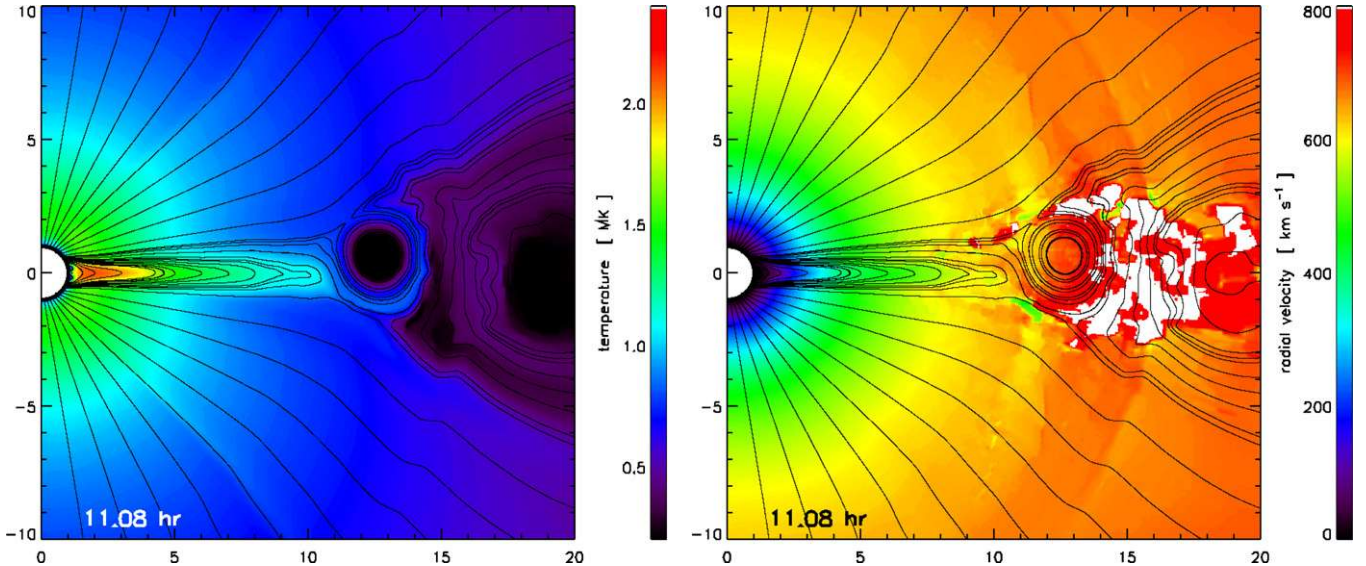


Figure 5. ARC7 magnetic breakout eruption at $t = 11.08$ hr showing the MHD proton temperature (left) and radial velocity (right) of the flux rope ejecta.

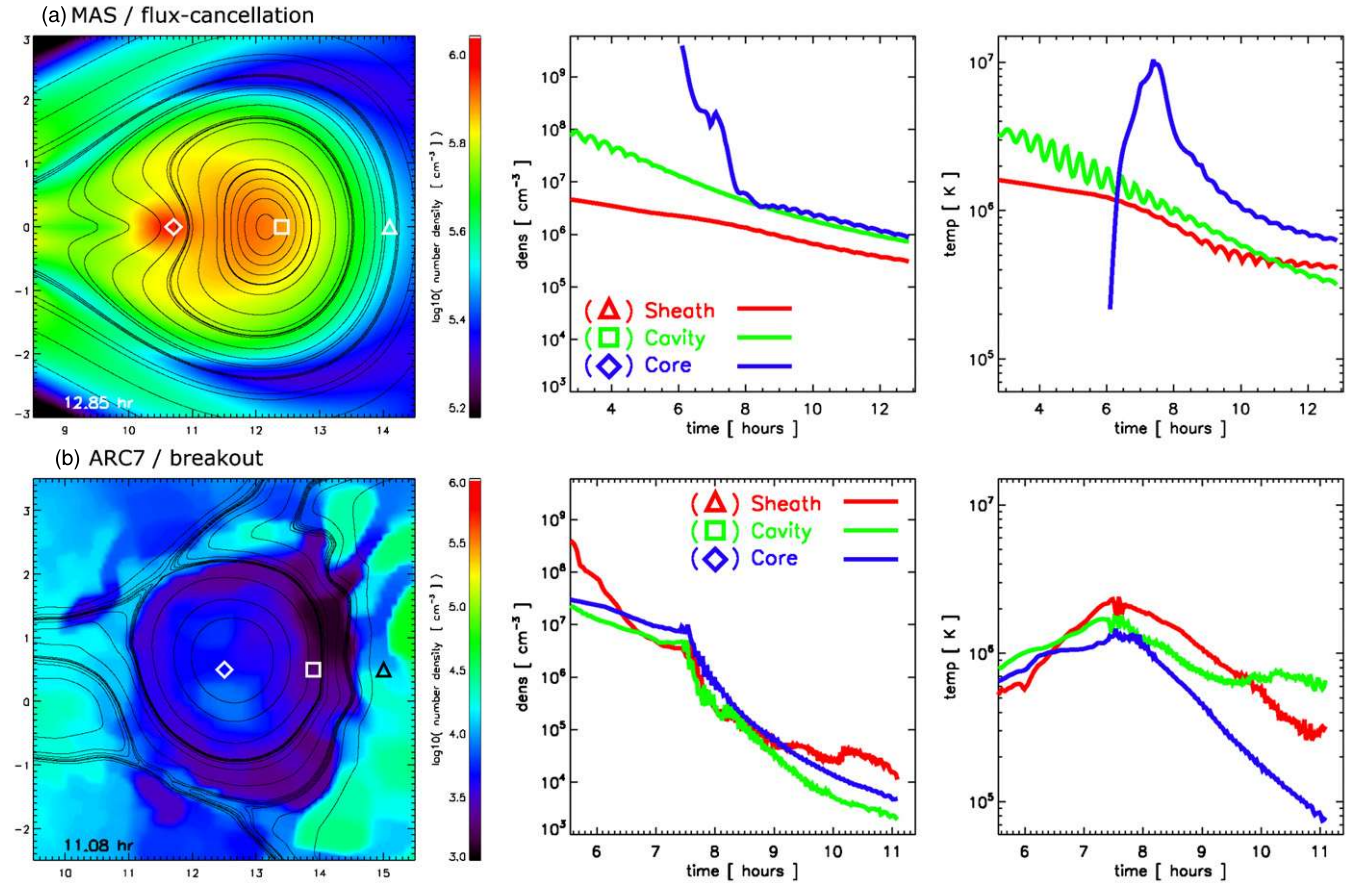


Figure 6. The top row (a) left panel plots the MHD proton number density on a log scale for the *MAS* flux-cancellation eruption at $t = 12.85$ hr. Also plotted are the spatial positions of three representative plasma parcels corresponding to the *sheath* (triangle), *cavity* (square), and *core* (diamond) regions. The center and right panels plot the number density and temperature evolution in time for each the three representative parcels: *sheath* (red), *cavity* (green), and *core* (blue), respectively. The bottom row (b) plots the proton number density from the *ARC7* magnetic breakout simulation at $t = 11.08$ hr and the representative plasma parcels' density and temperature histories in the same format as the top row.

row) simulation results. The left panels show the number density in each of the MHD simulation results for zoomed-in $6 R_{\odot} \times 6 R_{\odot}$ regions centered on the CME flux rope at times $t = 12.85$ hr and $t = 11.08$ hr for the flux-cancellation and breakout cases, respectively. For each simulation, we have

plotted three different starting points of our velocity integration routine, selected for their approximate correspondence to the *sheath* (triangle), *cavity* (square), and *core* (diamond) regions of the ejecta flux rope. Each individual parcel's integration backward in time is stopped when the parcel has reached a radial

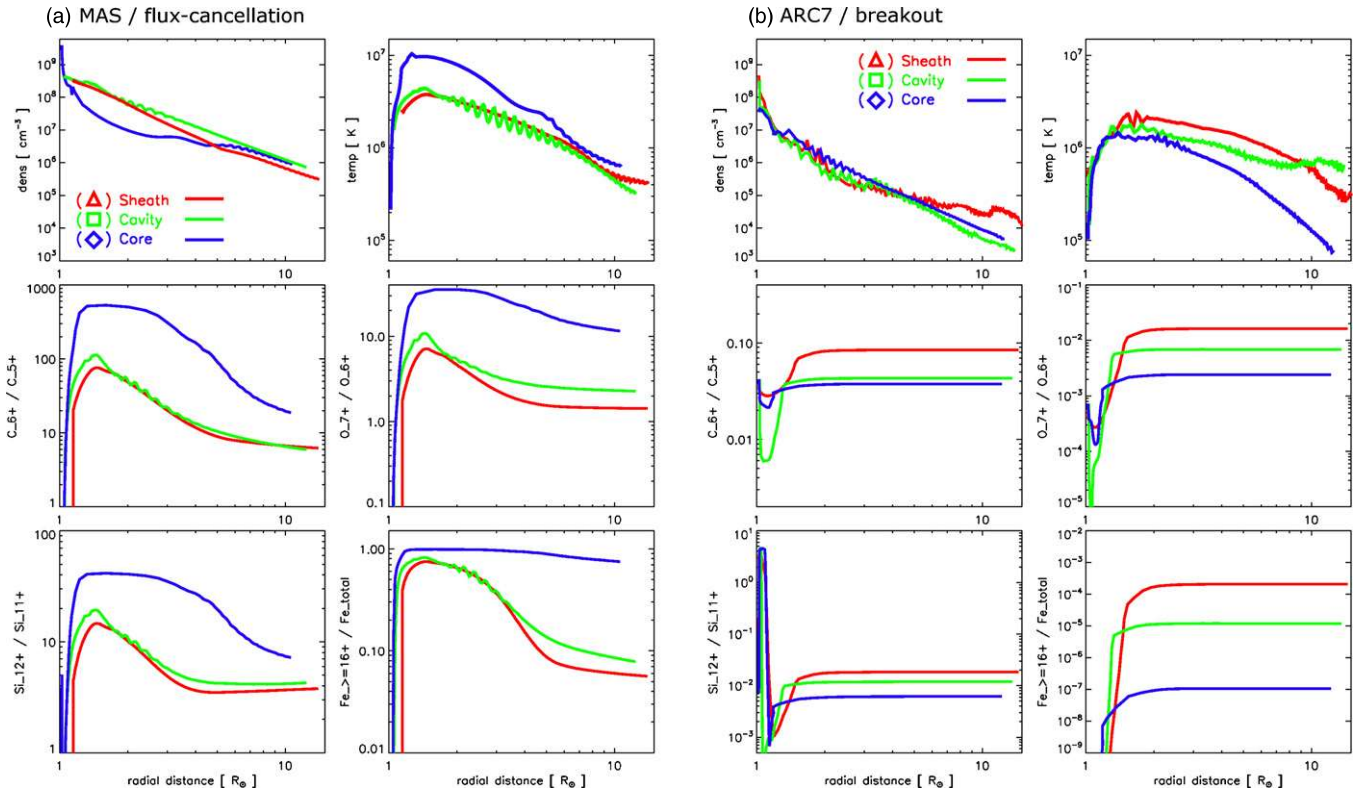


Figure 7. The top row of column (a) shows the *MAS* flux-cancellation density and temperature evolution of the plasma parcels in Figure 6 as functions of radial distance. The remaining plots in column (a) show the *BLASPHEMER* output of the radial evolution of the ionic charge state ratios C^{6+}/C^{5+} , O^{7+}/O^{6+} , Si^{12+}/Si^{11+} , and Fe^{24+}/Fe_{total} . Column (b) shows the corresponding *ARC7* magnetic breakout plasma parcels and their respective ionic charge state ratios.

distance of $\leqslant 1.01 R_\odot$ or the time of the MHD simulation data associated with achieving the steady-state solar wind solution, i.e., panel (a) in Figures 2 and 4. The center and right panels of Figure 6 in each row plot the temporal evolution of the density and plasma temperature for each of the Lagrangian plasma parcels until the simulation times shown in the left panels. The *sheath* parcels plotted in red, the *cavity* parcels in green, and the *core* parcels in blue. The axis scaling for the density and temperature plots is the same for the two simulations to ease the visual comparison between them. The top row of Figure 7 shows the density and temperature histories of these same representative parcels as a function of radial distance for the *MAS* simulation (plots in column (a)) and the *ARC7* simulation (plots in column (b)).

The differences between the two CME simulations are clearly evident in both the density and temperature histories of the sample plasma parcels and are most easily compared in the top row of Figure 7. While the initial plasma density at the inner boundary of the *sheath* and *cavity* parcels is comparable in the *MAS* and *ARC7* cases ($\sim 3\text{--}5 \times 10^8 \text{ cm}^{-3}$), the initial *core* densities differ by two orders of magnitude, $4 \times 10^9 \text{ cm}^{-3}$ in *MAS* versus $4 \times 10^7 \text{ cm}^{-3}$ in *ARC7*. The radial dependence of the density fall off is similar but the *ARC7 sheath* and *cavity* profiles have an initial steep drop off not seen in the corresponding *MAS* profiles. The *MAS core* parcel does show this initial drop-off, but levels out due to being a part of the higher density reconnection jet outflow. The temperature profiles in the *MAS* simulation show significantly more low corona heating in each of the plasma parcels than in the *ARC7* results. Specifically, the peak temperature experienced by the *MAS core* parcel from the flare reconnection reaches $\sim 10 \text{ MK}$ by $1.5 R_\odot$ and

maintains a $> 3 \text{ MK}$ temperature through $4 R_\odot$. The *ARC7 core* parcel reaches $\sim 1 \text{ MK}$ through $2.5 R_\odot$ and drops precipitously afterward. The *MAS sheath* and *cavity* parcels are $> 2 \text{ MK}$ until approximately $4 R_\odot$ (reaching $\sim 4 \text{ MK}$ at $1.5 R_\odot$), whereas the *ARC7 sheath* and *cavity* parcel temperatures are slightly cooler, i.e., $1\text{--}2 \text{ MK}$ over the same radial distance. An intriguing feature of the *ARC7* temperature profiles is the spread between the three representative parcels. Only the *core* parcel shows the adiabatic temperature decrease expected from an isolated plasmoid. The *sheath* material temperature profile has a much shallower slope related to compressional heating of the increased density pile-up at the leading edge of the ejecta from the streamer belt material. The *cavity* region temperature profile shows continuous heating through $\sim 14 R_\odot$ even though the density fall off is similar to that of the *core* parcel. This heating of the CME interior is a consequence of the continual breakout reconnection during the CME propagation through the low corona. As we will see in Section 4, the differences in the density and temperature histories of the CME material will result in very different ionic charge state signatures.

3.2. Solving the Time-dependent Ionization Equations

We use the MHD proton density and temperature time history of an individual plasma parcel to solve the time-dependent ionization equations for various minor heavy ion species acting as passive tracers of the bulk flow assuming at any given time the plasma is electrically neutral ($n_e = n_p$) and the electron temperature is the same as the proton temperature ($T_e = T_p$). The following calculation of the ionic charge states follows that of Rakowski et al. (2007, 2011) except here we have replaced

their semi-empirical analytic prescription of the density and temperature evolution of CME plasma with the results from the parcel tracing through the numerical MHD simulations.

In the frame of the Lagrangian plasma parcel, the number density n_q^i for a given heavy ion species i of charge $+q$ is given by

$$\frac{dn_q^i}{dt} = n_e [C_{q-1}^{\text{ion}} n_{q-1}^i - (C_q^{\text{ion}} + C_q^{\text{rr}} + C_q^{\text{dr}}) n_q^i + (C_{q+1}^{\text{rr}} + C_{q+1}^{\text{dr}}) n_{q+1}^i]. \quad (14)$$

Here, the right-hand side includes the sources and sinks for ions into or out of the charge state q , i.e., C_q^{ion} is the electron impact ionization ($q \rightarrow q+1$), and $C_q^{\text{rr}}, C_q^{\text{dr}}$ are the radiative recombination and dielectronic recombination, respectively ($q \rightarrow q-1$). We use a modified version of the *Blast Propagation in a Highly Emitting Environment* code (*BLASPHEMER*; e.g., Laming & Grun 2002; Laming & Hwang 2003; Rakowski et al. 2007) to integrate these sets of ionization balance equations in time for the heavy ion species carbon, oxygen, silicon, and iron. For the most up-to-date references for the ionization and recombination coefficients, see Section 3.1 of Rakowski et al. (2007). We calculate the fractionation of the individual charge states for a given ion as $n_q^i / \sum_q n_q^i$ to avoid the difficulty of having to specify the actual number density of the minor ion species which is obviously beyond the scope of our single-fluid MHD simulations. *BLASPHEMER* uses cubic spline interpolation in time to obtain the density and temperature between the points from the plasma parcel traces during the temporal integration. Example plots of the *BLASPHEMER* output for individual ion charge states, their evolution, and freeze-in can be found in Rakowski et al. (2007) and visualizations of the radial evolution of several heavy ion's entire charge state distributions can be found in Gruesbeck et al. (2011).

The lower four panels in Figure 7 plot the calculated carbon ($\text{C}^{6+}/\text{C}^{5+}$), oxygen ($\text{O}^{7+}/\text{O}^{6+}$), silicon ($\text{Si}^{12+}/\text{Si}^{11+}$), and iron ($\text{Fe}^{\geq 16+}/\text{Fe}_{\text{total}}$) ionic charge state ratios and their evolution with radial distance for the *sheath*, *cavity*, and *core* traces discussed earlier for both the *MAS* flux-cancellation (panels in column (a)) and *ARC7* breakout (panels in column (b)) simulations. The differences in the density and temperature evolution of these representative parcels result in the freeze-in of the calculated ionic charge states occurring over a range of radial values. In these plots, the charge states can be considered frozen-in at the distances where the curves level-off and start approaching an asymptotic value. The *MAS* *sheath* and *cavity* parcel charge state ratios appear to be freezing in at roughly $4-5 R_\odot$. However, it is not clear that the *MAS* *core* parcel's charge state ratios have frozen in at all by the end of the simulation ($10 R_\odot$). In contrast, the *ARC7* parcel charge state quantities all freeze in very low down ($< 2 R_\odot$, i.e., very early on once the eruption is underway) and remained fixed throughout the remainder of the eruption propagation.

It is worth noting that Rakowski et al. (2007, 2011) discuss how one could calculate both the ion (T_i) and electron (T_e) temperatures separately to utilize specific ion or electron heating terms and take into account their temperature coupling due to Coulomb collisions. The temperature of heavy ions measured in the heliosphere is generally mass proportional with $T_i \sim m_i T_p$ (von Steiger & Zurbuchen 2006). In the source regions of fast solar wind acceleration, where energy deposition from wave dissipation is likely to preferentially heat certain heavy ions, the temperature ordering of minor ions, protons, and electrons

is $T_i \gg T_p > T_e$ (e.g., Ofman 2004). However, the situation in the slow solar wind acceleration region is not necessarily as straightforward. For example, David et al. (1998) measured T_e in the quiet (closed field/helmet streamer) corona above the equatorial west limb ($1.05 \leq r/R_\odot \leq 1.35$) and showed it increasing from 1 to 3.5 MK with radial distance—a factor of 1.5–6 times higher than T_e above a coronal hole. Newbury et al. (1998) showed that in the heliosphere at 1 AU the electron temperature is consistently greater than the proton temperature for slow and moderate bulk speeds, with averages ranging from $\langle T_e/T_p \rangle \sim 4$ at 300 km s^{-1} to $\langle T_e/T_p \rangle \sim 1$ by 600 km s^{-1} and only dropping below unity in the fast wind, $\langle T_e/T_p \rangle \sim 0.5$. In light of the fact that some solar wind models predict $T_e > T_p$ and some $T_e < T_p$ in the range of heliocentric distances of interest to our problem (before charge state freeze-in $\lesssim 6 R_\odot$), our simplification of equating the electron temperature with the single-fluid MHD proton temperature, $T_e = T_p$, represents a fairly reasonable compromise.

4. SPATIAL DISTRIBUTION OF CHARGE STATES IN THE CME FLUX ROPES

The spatial distribution of ionic charge states within CMEs, specifically in relation to or in the context of their magnetic structure, has been suggested as a possible means for determining the CME initiation mechanism (e.g., Lynch et al. 2003a, 2003b; Riley et al. 2004; Lin et al. 2004). Using the procedure described in the previous section, we have generated 3600 individual plasma parcel traces for each of the simulations to determine density and temperature profiles and used these as inputs into the *BLASPHEMER* code to calculate the temporal evolution of the C, O, Si, and Fe charge state distributions. The initial starting points of the parcel tracing sample the $6 R_\odot \times 6 R_\odot$ regions centered on the CME flux rope ejecta (precisely the region shown in Figure 6) in a regular 60×60 grid. These simulation times (*MAS*: $t = 12.85 \text{ hr}$, *ARC7*: $t = 11.08 \text{ hr}$) were selected when the center of the magnetic flux ropes had reached $\sim 12 R_\odot$. We use the *BLASPHEMER* charge state distributions to calculate pixel maps for the commonly observed charge state ratios plotted in Figure 7.

4.1. MAS Flux-cancellation Results

The ionic charge state ratios derived from the *MAS* simulation results are presented in Figure 8. Panel (a) plots $\text{C}^{6+}/\text{C}^{5+}$, (b) $\text{O}^{7+}/\text{O}^{6+}$, (c) $\text{Si}^{12+}/\text{Si}^{11+}$, and (d) $\text{Fe}^{\geq 16+}/\text{Fe}_{\text{total}}$. The ionic charge states show a common spatial structure; there are regions of elevated charge states in the process of forming a ring-like structure around the central region of the magnetic flux rope. This enhanced ring-like structure is most visible (and uniform) in the hot iron ratio (panel (d)) but is also present, with additional spatial variation, in each of the other charge state quantities. Lin et al. (2004) suggested, in a similar 2.5D loss-of-equilibrium CME scenario, that as the flare-heated plasma and the newly reconnected magnetic field becomes part of the erupting structure one might expect that the outer layers of the flux rope are hotter than the inner part. We see that here both in the MHD temperature directly (Figure 3) and in the enhanced charge state ratios.

Quantitatively, *MAS* flux-cancellation $\text{O}^{7+}/\text{O}^{6+}$ and $\text{Fe}^{\geq 16+}/\text{Fe}_{\text{total}}$ charge state ratios in the enhanced ring-like structure are consistent with the values obtained with in situ observations of magnetic cloud ICMEs. Lynch (2006) showed that, within “fast” magnetic clouds (average radial speed of $\geq 500 \text{ km s}^{-1}$),

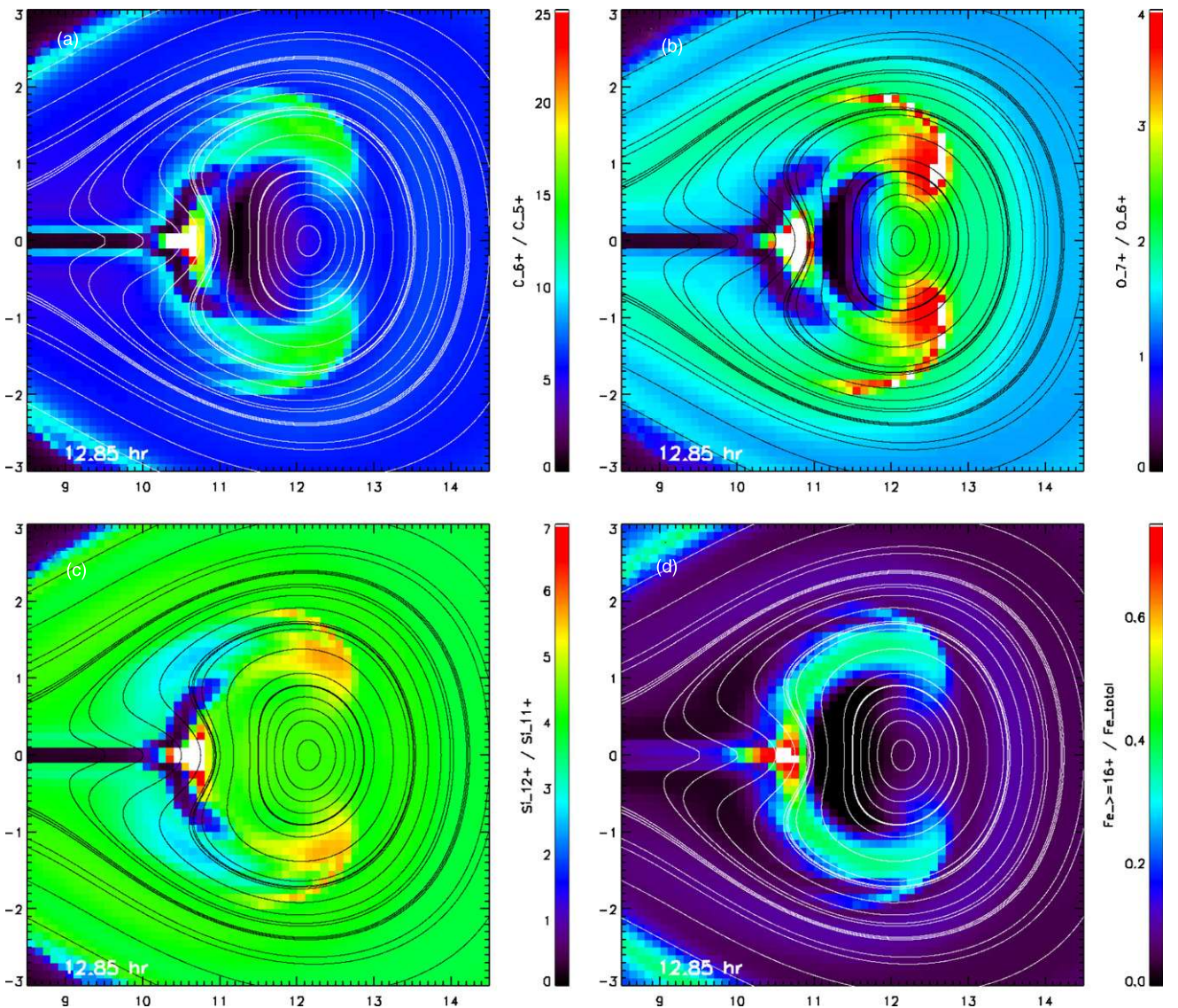


Figure 8. Spatial distributions of commonly measured heavy ion charge state ratios for the *MAS* flux-cancellation CME at $t = 12.85$ hr plotted with representative magnetic field lines. Panel (a) shows C^{6+}/C^{5+} , (b) O^{7+}/O^{6+} , (c) Si^{12+}/Si^{11+} , and (d) $Fe^{>16+}/Fe_{total}$. Each panel plots the charge state ratios in 60×60 pixel bitmaps corresponding to 3600 individual Lagrangian plasma parcels tracked through the MHD simulation data.

the mean high oxygen charge state ratio $\langle O^{7+}/O^{6+} \rangle$ was ~ 2.1 and the mean high iron charge states were $\langle Fe^{>16+}/Fe_{total} \rangle \sim 0.40$. The Lynch (2006) in situ observations within “slow” magnetic clouds (average radial speeds of < 500 km s $^{-1}$) gave mean values of $\langle O^{7+}/O^{6+} \rangle \sim 1.2$ and $\langle Fe^{>16+}/Fe_{total} \rangle \sim 0.21$. The *MAS* charge state ratios in Figure 8 are certainly elevated above the nominal distributions found in the slow solar wind; for example, Zurbuchen et al. (2000) showed that the long-term average of slow solar wind gave $\langle O^{7+}/O^{6+} \rangle \sim 0.39 \pm 0.13$.

The enhanced ring-like structure in the *MAS* simulation results is the direct consequence of the reconnection heated material being supplied to the CME by the reconnection jet outflow. As the ejecta continues to propagate this heated plasma flows along the magnetic field lines (flux surfaces in our 2.5D simulations) from the back of the flux rope toward the front showing the continued dynamic evolution of the flare-heated plasma in the interior of the CME’s magnetic structure. Additionally, the reconnection jet outflow itself is creating a compression region that both distorts the magnetic field structure and provides some additional heating resulting in a localized

charge state hot spot at the rear of the ejecta (again, the color white indicates values higher than the maximum of the color scale). The *MAS* charge states agree with the results of the statistical survey by Reinard (2008) who showed that ionic charge states were more enhanced in events where the spacecraft sampled the center of the ICME rather than its flanks (using the CME source location as a proxy for the relative ICME and spacecraft positioning).

The spatial structure of the enhanced charge states within the ejecta also show some resemblance to the simulation results of Shiota et al. (2005). Those authors examined the evolution of the density, pressure, and temperature during a similar flux rope eruption and showed how various plasma properties propagate out of the flare reconnection region through the ejecta in the form of slow mode shock fronts, spiraling around the flux surfaces from the rear of the flux rope ejecta to the front and back around again. Our results, while quantitatively different, do show similar structure of the propagation of the flare-heated material (i.e., the MHD temperature) and the enhanced ionic charge state signatures (associated with having been part of the

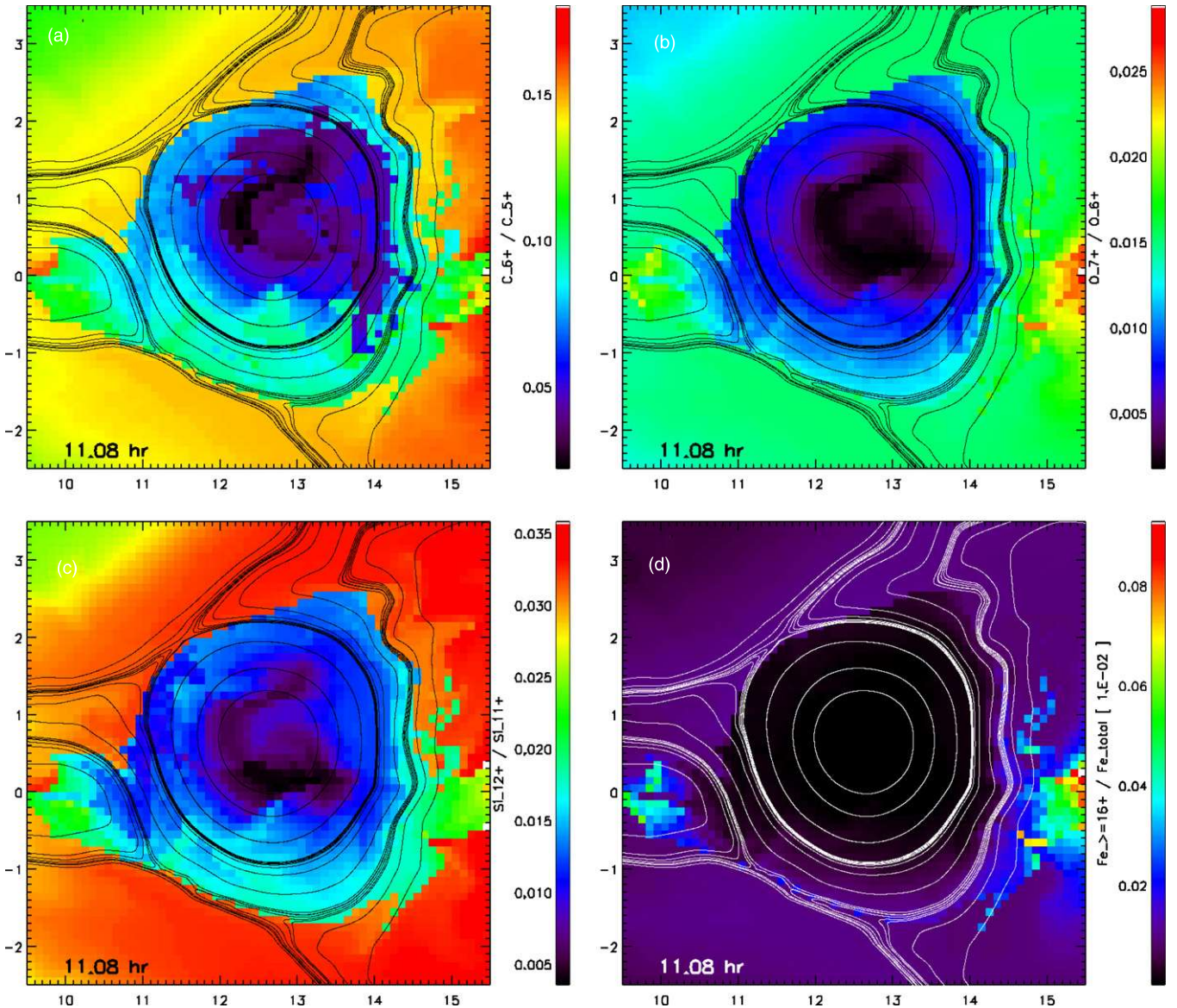


Figure 9. Spatial distribution of commonly measured heavy ion charge state ratios for the *ARC7* magnetic breakout CME at $t = 11.08$ hr plotted in the same format as Figure 8.

flare reconnection jet) throughout the ejecta. The Shiota et al. (2005) simulations also show a density rarefaction region in the ejecta that we do not see (compare their Figure 9 to our Figures 3 and 6), but their rarefaction region does correspond to the region of relatively low values in our carbon, oxygen, and iron charge states.

4.2. *ARC7* Magnetic Breakout Results

Figure 9 shows the simulation ionic charge state structure for the *ARC7* breakout flux rope in the same format as Figure 8. Once again, the carbon, oxygen, silicon, and iron charge state ratios show a common structure. However, the *ARC7* charge states differ from the *MAS* results in two important ways. First, the lowest values for all of the charge state ratios are at the center of the magnetic flux rope. There is overall less symmetry in the *ARC7* flux rope solution by $\sim 12 R_\odot$, but the spatial structure includes layers (flux surfaces) of increasing charge state values as one moves toward the edge of the ejecta. In fact, the highest charge state values are exterior to the magnetic ejecta entirely.

Second, the magnitude of all the *ARC7* charge state ratios is much lower than their *MAS* counterparts, by roughly a factor of 100–200 in the C, O, and Si ratios and $\gtrsim 10^3$ in Fe.

The *ARC7* simulation results are similar to those obtained in the recent study by Gruesbeck et al. (2011) for their fast heating, low density case. Comparing their density and temperature profiles (see Figure 5 of Gruesbeck et al. 2011) with the density and temperature radial evolution for the *ARC7* representative plasma parcels in Figure 6 shows both the quantitative and qualitative similarities—a rapid rise to 1–2 MK temperatures while simultaneously having relatively low plasma densities ($\lesssim 10^7 \text{ cm}^{-3}$) during the first few solar radii of evolution. Since the *ARC7* breakout profiles result in almost no enhanced charge states for any of our ions of interest, C^{6+} , O^{7+} , Si^{12+} , or $\text{Fe}^{\geq 16+}$, the charge state ratios plotted in Figure 9 are obviously much lower.

One of the positive aspects of the much lower charge states derived from the *ARC7* solution is that the effect of the in situ CME heating, as mentioned in Section 3.1, is clearly visible. While the *ARC7* code has no explicit magnetic resistivity, the

effective numerical resistivity is obviously sufficient to maintain continual breakout reconnection during the propagation of the ejecta. Rakowski et al. (2011) have recently modeled this effect as resistive dissipation of magnetic energy during a spheromak expansion to try to explain the moderate charge states seen in the interior of the 2007 May 19 CME observed by *STEREO*. The field lines in the *ARC7* plots show the topological configuration of the CME and its relation to the background solar wind. The original overlying current sheet responsible for the breakout reconnection now encompasses the entire ejecta and the null point has split into two X-point regions on the sides and a little behind the flux rope proper. There is an interaction region surrounding the flux rope that shows higher charge states than the CME interior. In fact, the *ARC cavity* parcel in Figure 6 is right in the middle of this interaction layer. The combination of the CME density being too low and the magnetic energy dissipated by the numerical resistivity not being entirely accounted for means, in this particular simulation, that the extended in situ heating does not have much of an effect on the charge states after $\sim 2\text{--}3 R_\odot$. Despite these limitations, the fact that there is a charge state imprint of this feature of the eruption motivates further investigation into these processes.

5. DISCUSSION

We have demonstrated a post-processing procedure for the calculation of heavy ion charge states from single-fluid MHD numerical simulations that yield reasonable ionic charge state results without having to develop a multi-fluid MHD formalism or solve the ionization and recombination equations for representative ion species directly in the MHD code at every time step. The procedure is robust enough to be easily applied to basically any MHD data set with moderate temporal cadence, and we have presented the results from two different axisymmetric CME eruptions run on the *MAS* and *ARC7* MHD codes. Our results represent an important advance in terms of our ability to constrain the MHD models of the steady-state solar wind, CME initiation, and CME/ICME propagation. In addition to the MHD simulation magnetic field and bulk (proton) plasma properties that are currently compared to in situ measurements at 1 AU, we can now add the heavy ion charge state composition to the list of simulation predicted outputs.

The CME simulations presented here are representative of the two dynamical types of CMEs as described by Low & Zhang (2002). These authors argued that the magnetic topology of the “inverse” configuration (cf. the *MAS* flux-cancellation simulation) gives rise to a slow CME and the topology of the “normal” configuration (cf. the *ARC7* magnetic breakout simulation) would predict a fast CME. However, subsequent surveys by Li & Luhmann (2006) and Ugarte-Urra et al. (2007) of CME source region topologies determined that both bipolar/“inverse” and multi-polar/“normal” flux systems produce fast CMEs without any significant statistical differentiation or preference. What the magnetic topologies of our two simulations do provide is essentially the two limiting cases of the relative contribution of the eruptive flare to what becomes the CME/ICME plasma: (1) the *MAS* flux-cancellation simulation results in a large radially extended eruptive flare current sheet that provides a constant source of flare-heated plasma via the reconnection jet to the CME eruption. The *MAS* ionic charge state structure completely reflects this property of the eruption and (2) the *ARC7* breakout simulation results in a relatively small and quickly dissipated eruptive flare current sheet, thus the CME is cut off from

the flare-heated material early in its evolution. The magnetic topology of the CME itself, the presence of the separatrix and current sheet surrounding the flux rope, and the continual breakout reconnection during the propagation result in the in situ heating of the ejecta and surrounding solar wind material. Both of these eruption features are also reflected in the *ARC7* ionic charge state structure.

Taken together, our simulation results show the exact opposite trend to what is observed in the in situ ICME charge state measurements, i.e., the relatively slow *MAS* CME has extremely elevated charge states and the relatively fast *ARC7* CME shows no enhancement at all. As discussed earlier, the fast/slow classifications of the simulation CMEs are not as straightforward as simply comparing the simulation velocities; a direct quantitative comparison of the two simulations is not appropriate at this stage because the background solar wind profiles, temperatures, and densities (and consequently the Alfvén speed) are very different in the two simulations and neither simulation was run with the goal of attempting to create realistic ionic charge state composition in the ejecta.

The analysis outlined herein, the unification of MHD modeling of CME initiation and propagation in the low corona with the time-dependent modeling of the charge state distributions of heavy ion species, can obviously be refined and improved in future work. The first improvement is a more realistic treatment of the electron temperature T_e . Clearly, our $T_e = T_p$ simplification does not take into account all of the physics associated with coronal heating and solar wind acceleration. However, this does not mean that we have to abandon the single-fluid MHD formalism. If an empirical relationship between the electron and proton temperatures were derived from observations or from detailed one-dimensional solar wind modeling, perhaps as a function of solar wind speed, then the same post-processing procedure for the calculation of ionic charge states could still be easily applied. Under certain MHD density and proton temperature conditions, we are able to generate relatively enhanced heavy ion charge states in the CME/ICME interior associated with the outflow of flare-heated plasma during the eruption. In this respect, our results are quite promising and have the potential to greatly improve the value of existing MHD solar and heliospheric modeling and modeling infrastructure.

The second obvious improvement is that the numerical MHD simulations need to be extended to fully three-dimensional systems. In fact, both the magnetic breakout and flux-cancellation CME initiation models have been run in one form or another in fully three-dimensional MHD codes (e.g., DeVore & Antiochos 2008; Lynch et al. 2008; Roussev et al. 2004, 2007; Linker et al. 2009; Amari et al. 2010). However, the three-dimensional versions are still very much under development, both in terms of various forms of the coronal heating and solar wind acceleration and in terms of the mechanisms for magnetic energy accumulation, storage, and rapid release via CME initiation and the associated eruptive flare reconnection. Specifically, the momentum and energy equations (4) and (5) can be improved to include more physics, better thermodynamics, and minimize the energy loss from numerical dissipation. Reeves et al. (2010) present an energy diagnostic during the *MAS* simulation described herein and shows a $\sim 4\%$ loss in total energy over the course of the entire simulation. These authors also examined the energy partition and transfer through the flare reconnection current sheet into both the closed flare loops below the eruption and into the ejecta. The *MAS* simulation’s prediction of elevated charge states that are consistent with observed in situ values is

evidence that we are making progress toward getting this partition right. Similar energy diagnostics need to be performed in the *ARC7* case and used to correct for the magnetic energy lost from the numerical diffusion in regions susceptible to magnetic reconnection—this energy should be converted into bulk plasma heating. It is clear that MHD numerical simulations are becoming increasingly sophisticated and will eventually be able to bridge the gap between lower corona spectroscopic observations and *in situ* ionic composition measurements.

In a fully three-dimensional system, the connection of the CME/ICME magnetic field to the simulation’s solar surface is maintained throughout the eruption (e.g., Lynch et al. 2008). Thus, the field-aligned thermal conduction can continue to supply the ejecta interior plasma with coronal temperature heat flux, somewhat mitigating the effects seen in Figure 6 of the temperature evolution of isolated, fully detached expanding plasmoids. However, it is not clear that the electron heat flux alone can account for the thermal heating required to model the observed UVCS emission in CME plasmas (e.g., Lee et al. 2009, and references therein).

An additional consequence of moving toward a three-dimensional eruption might be an increased mixing of various constituent plasmas of the CME. We have seen in Figure 8 a snapshot of the spatial distribution of the high charge state material and how that spatial distribution is still evolving. The heavy ion charge states remain frozen-in but from the ejecta’s magnetic structure, we can easily deduce that the ring of enhancement will continue to spread itself out along the CME/ICME flux surfaces as required by the 2.5D symmetry. In three dimensions, the spatial structure of the ejecta plasma is likely to exhibit significantly more complexity and variation, not only over the flux rope cross section, but also potentially along the flux rope’s azimuthal extent.

Detailed, multi-wavelength remote sensing analyses of individual CMEs in the low corona have started to reveal some of the complex three-dimensional structure in specific events. For example, Landi et al. (2010) analyzed the 2008 April 9 CME combining *Hinode*/EIS and *SOHO*/UVCS spectroscopic measurements of the core plasma and *Hinode*/XRT observations of the flare-heated plasma. They found emission from the core region of the CME to be consistent with plasmas of varying temperatures from 5×10^4 to 6×10^5 K and faint *Hinode*/XRT emission corresponding to plasma temperatures of 5–10 MK that “enveloped [the cooler core plasma] like a cup.” The Landi et al. (2010) results show a qualitatively similar scenario to earlier UVCS observations by Akmal et al. (2001) that analyzed the co-spatial emission of a cool knot of core material (6×10^4 K) within a warmer loop-like structure (4×10^5 K). The spatial structure of our *MAS* enhanced charge state results, extrapolated to three dimensions, could either resemble a cup or an arcade-like Y-feature beneath the center of the erupting flux rope (e.g., Shiota et al. 2005), potentially in agreement with the multi-temperature UVCS observations.

In the heliosphere, multipoint *in situ* observations can also be used to unravel some of the three-dimensional spatial structure and variation of ionic charge states within ICMEs. Until recently, there have been only a handful of well-observed multi-spacecraft ICME observations (e.g., Burlaga et al. 1981; Mulligan et al. 1999; Mulligan & Russell 2001) and these have rarely had composition data (Riley et al. 2003). Now that the *STEREO* spacecraft are in quadrature with *SOHO* and *ACE*, we can directly compare the remote sensing imaging from one spacecraft with the *in situ* plasma properties at another

(e.g., Rouillard et al. 2009; Möstl et al. 2009; Lynch et al. 2010). This should allow us to more concretely place regions of high (or low) charge states within the context of the ICME magnetic structure along the lines of the analysis by Reinard et al. (2010) who presented multipoint average iron charge state (Q_{Fe}) measurements in a couple of *STEREO* ICME events.

The analysis presented herein should help us both constrain the coronal heating and solar wind parameterization in the MHD models as well as start to unravel the complex temperature structure, its spatial variation, and temporal evolution during CME initiation and propagation. Once the MHD simulations of CME initiation and eruption are consistent with both the observed UV emission in the low corona and *in situ* heavy ion charge states within the ejecta (at simulation distances after the charge states have frozen in) then we ought to be reasonably confident that the numerical simulations are capturing the most essential physics associated with the energy partitioning and bulk flare heating during the eruption.

B.J.L. thanks S. K. Antiochos and G. H. Fisher for helpful discussion during the preparation of the manuscript. This collaborative research was made possible with support from NASA’s Heliosphysics Theory, Guest Investigator, Living With a Star, and SR&T programs, as well as the NSF SHINE program, the Office of Naval Research, and the Center for Integrated Space Weather Modeling (an NSF Science and Technology Center). B.J.L. and Y.L. acknowledge support from NASA HTP NNX08AJ56G NNX11AJ65G, and NASA HGI NNX08AJ04G; A.A.R. and T.L.M. acknowledge NASA SR&T NNX08AH54G; C.E.R. and J.M.L. acknowledge NASA HGI NNG08EK62I and basic research funds of the Office of Naval Research; K.K.R. acknowledges NSF SHINE ATM0752257; and J.C.A. and P.J.M. acknowledge support from NASA TR&T NNG04GN00G.

REFERENCES

- Akmal, A., Raymond, J. C., Vourlidas, A., et al. 2001, *ApJ*, **553**, 922
- Allred, J. C., & MacNeice, P. J. 2011, *J. Geophys. Res.*, submitted
- Amari, T., Aly, J. J., Mikić, Z., & Linker, J. 2010, *ApJ*, **717**, L26
- Antiochos, S. K., DeVore, C. R., & Klimchuk, J. A. 1999, *ApJ*, **510**, 485
- Athay, R. G. 1986, *ApJ*, **308**, 975
- Bame, S. J., Asbridge, J. R., Feldman, W. C., Fenimore, E. E., & Gosling, J. T. 1979, *Sol. Phys.*, **62**, 179
- Bemporad, A., Raymond, J. C., Poletto, G., & Romoli, M. 2007, *ApJ*, **655**, 576
- Bochsler, P. 2000, *Rev. Geophys.*, **38**, 247
- Bürgi, A. 1992, *J. Geophys. Res.*, **97**, 3137
- Bürgi, A., & Geiss, J. 1986, *Sol. Phys.*, **103**, 347
- Burlaga, L. F., Fitznerreiter, R., Lepping, R., et al. 1998, *J. Geophys. Res.*, **103**, 277
- Burlaga, L. F., Sittler, E., Mariani, F., & Schwenn, R. 1981, *J. Geophys. Res.*, **81**, 6673
- David, C., Gabriel, A. H., Bely-Dubau, F., Lemaire, P., & Wilhelm, K. 1998, *A&A*, **336**, L90
- DeVore, C. R., & Antiochos, S. K. 2008, *ApJ*, **680**, 740
- Evans, R. M., Opher, M., Manchester, W. B., IV., & Gombosi, T. I. 2008, *ApJ*, **687**, 1355
- Fenimore, E. E. 1980, *ApJ*, **243**, 245
- Galvin, A. B. 1997, in Coronal Mass Ejections, ed. N. Crooker, J. A. Joselyn, & J. Feynman (Geophysical Monograph, Vol. 99; Washington, DC: AGU), 253
- Gloeckler, G., Fisk, L. A., Hefti, S., et al. 1999, *Geophys. Res. Lett.*, **26**, 157
- Gloeckler, G., Geiss, J., Balsiger, H., et al. 1992, *A&AS*, **92**, 267
- Gruesbeck, J. R., Lepri, S. T., Zurbuchen, T. H., & Antiochos, S. K. 2011, *ApJ*, **730**, 103
- Hansteen, V. H., Leer, E., & Holzer, T. E. 1997, *ApJ*, **482**, 498
- Henke, T., Woch, J., Mall, U., et al. 1998, *Geophys. Res. Lett.*, **25**, 3465
- Henke, T., Woch, J., Schwenn, R., et al. 2001, *J. Geophys. Res.*, **106**, 10957
- Hollweg, J. V. 1978, *Rev. Geophys. Space Phys.*, **16**, 689

